The Astrophysical Journal Letters, 873:L11 (9pp), 2019 March 10 https://doi.org/10.3847/2041-8213/ab07bd

Mega-Gauss Plasma Jet Creation Using a Ring of Laser Beams

L. Gao[1], E. Liang[2], Y. Lu[2,3], R. K. Follet[4], H. Sio[5], P. Tzeferacos[6], D. H. Froula[4], A. Birkel[5], C. K. Li[5], D. Lamb[6], R. Petrasso[5], W. Fu[2], M. Wei[7], and H. Ji[1]
[1] Princeton Plasma Physics Laboratory, Princeton University, Princeton, NJ 08536, USA
[2] Rice University, Houston, TX 77005, USA; liang@rice.edu
[3] Los Alamos National Laboratory, Los Alamos, NM 87545, USA
[4] Laboratory for Laser Energetics, Rochester, NY 14623, USA
[5] Plasma Science and Fusion Center, Massachusetts Institute of Technology, Cambridge, MA 02139, USA
[6] Department of Astronomy and Astrophysics, University of Chicago, Chicago, IL 60637, USA
[7] Laboratory for Laser Energetics, University of Rochester, Rochester, NY 14623, USA
Received 2019 January 13; revised 2019 February 12; accepted 2019 February 13; published 2019 March 8

Abstract

Using 20 OMEGA laser beams at the Laboratory for Laser Energetics, University of Rochester, to irradiate a flat plastic target in a hollow ring configuration, we created supersonic cylindrical stable plasma jets with self-generated megagauss magnetic fields extending out to >4 mm. These well-collimated magnetized jets possess a number of distinct and novel properties that will allow us to study the dynamics, physical processes, and scaling properties of astrophysical jets with a dynamic range exceeding those of previous laboratory settings. The dimensionless parameters of these laboratory jets fall in the same regime as those of young stellar object jets. These jets will also provide new versatile laser-based platforms to study magnetized shocks, shear flows, and other plasma processes under controllable conditions.

Key words: hydrodynamics – magnetic fields – stars: jets

1. Introduction

Magnetized plasma jets are ubiquitous in the universe (Ferrari 1998; Livio 1999; Sari et al. 1999; Bally et al. 2007; Frank et al. 2014). It is thus highly desirable to recreate them in the laboratory to study their physical processes and scaling properties under controllable conditions. Recently, the irradiation of solid targets with high-energy lasers has become a popular tool to launch supersonic plasma outflows for a broad range of applications, including the study of astrophysical jets (see articles in Hartigan 2013; Ciardi 2015).

When an intense laser irradiates a solid target, strong toroidal magnetic fields are created around the laser spot by the $\nabla P_e \times \nabla n_e$ term ("Biermann battery," where P_e = electron pressure, n_e = electron density, Biermann 1950) of the generalized Ohm's law (Krall & Trivelpiece 1973; Epperlein 1984; Epperlein & Haines 1986). However, these magnetic fields are localized at the surface, spanning distances $\leqslant$ a few times laser spot size. They decay rapidly in time and space as the outflow expands, diverges, and rarifies. Hence the creation of stable cylindrical plasma jets with strong self-generated magnetic fields at large distances from the laser target remains an unsolved challenge. Here we report a new laser platform capable of creating stable cylindrical plasma jets with megagauss (MG) self-generated fields extending to >4 mm, by using 20 OMEGA laser beams with 10 kJ total energy at the Laboratory for Laser Energetics (LLE; Boehly et al. 1995) of the University of Rochester, to irradiate a flat CH target in a hollow ring pattern. We use CH as the baseline target material because its radiative cooling effect is small and dynamically unimportant. For comparison we also added high-Z dopant to the CH target to study the effects of radiative cooling on jet properties (see Section 3).

The goal of our laser experiment is to create hydrodynamic collimated jets with the strongest self-generated magnetic fields extending to the largest distance from target. Hence it is useful to first review some of the previous laboratory jet experiments. Large-scale magnetized jets had been previously created using pulse power machines by many groups (Lebedev et al. 2002, 2005; Gourdain et al. 2010; Suzuki-Vidal et al. 2011). These jets mostly consist of low-density plasmas ($n_e \leqslant 10^{19}\mathrm{cm}^{-3}$) accelerated by externally induced $\boldsymbol{j}\boldsymbol{x}\boldsymbol{B}$ forces ($\boldsymbol{j}$ = current, $\boldsymbol{B}$ = magnetic field) and collimated by strong toroidal fields. Therefore, their dynamics and physical properties are fundamentally different from those of hydrodynamic jets launched by laser-solid-target interactions.

Beginning in the 1990s, laser-driven hydrodynamic jets have been created by irradiating cone-shaped or V-shaped foil targets to thermalize the transverse momentum and facilitate axial collimation of the outflow (Farley et al. 1999; Gregory et al. 2008). A series of experiments to study radiative jet formation and interaction with ambient material was conducted by the group at the Prague Asterix Laser System (PALS), by varying the focal spot size of a single laser beam irradiating different flat metal targets (Kasperczuk et al. 2006; Nicolaï et al. 2006, 2008; Pisarczyk et al. 2007; Tikhonchuk et al. 2008). In all these early laser-driven hydrodynamic jet experiments, collimation were achieved by radiative cooling and radial collapse, and no magnetic field measurements were made. Though the laser intensity profile of the PALS experiments became concave and ring-like as the focal spot radius was increased, these authors firmly established that the primary factor in their jet collimation was radiative cooling and radial collapse (Kasperczuk et al. 2006; Nicolaï et al. 2006). Detailed numerical simulations of the PALS experiments also found that no significant magnetic field was created far from the target (Nicolaï et al. 2006). This is expected as the electron pressure and density gradients interior to the single laser spot are insufficient to create strong Biermann-battery fields far away from the target surface. FLASH simulations clearly show that to create strong Biermann-battery fields far from the laser target, one needs a hollow ring radius $\ll$ the width of the ring, which was not the case in the PALS experiments, where the laser spot size and annular width were comparable.

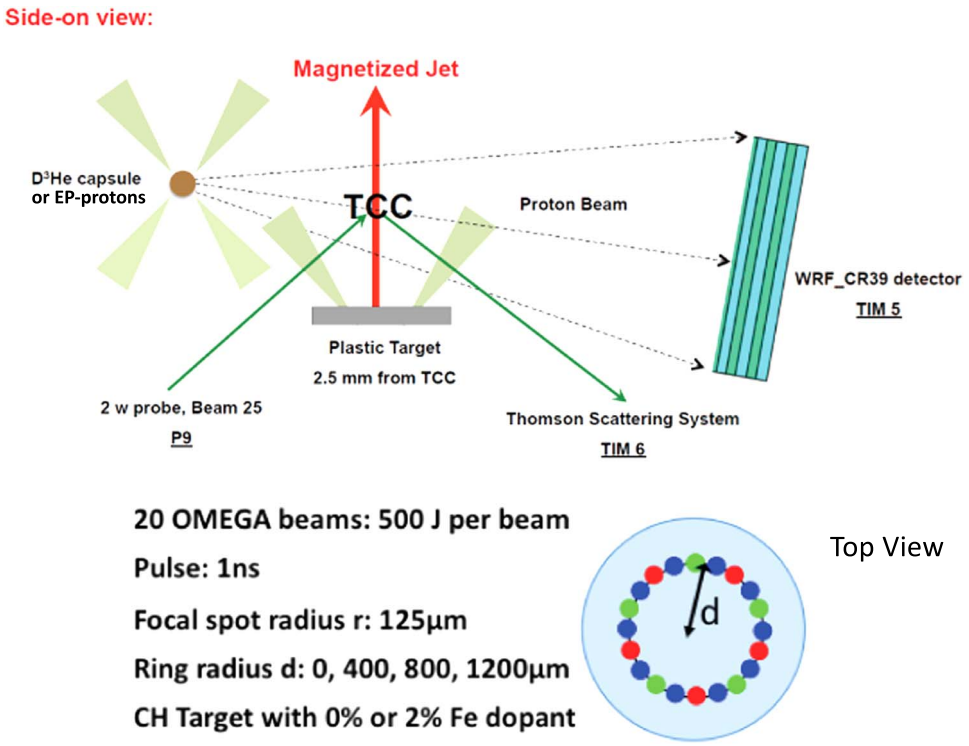

Figure 1. Setup of the OMEGA magnetized jet experiment. Laser parameters and top view of 20-beam pattern (colors denote different incident angles) are illustrated in the lower figure. The CH target is located 2.5 mm below target chamber center (TCC). D^3He or OMEGA-EP proton sources are located ~1 cm to the left of TCC and proton images are recorded at 16.5–17 cm to the right of TCC. A $2\omega_o$ TS probe beam measured plasma parameters at TCC with ~50 μm spatial resolution. Not shown is the XRFC, which looks down at ~38° from the jet axis.

More recently, a strongly magnetized jet-like outflow was created using two OMEGA laser beams to irradiate a V-shaped foil, such that the collision of the two blow-offs leads to the reconnection and advection of their combined Biermann-battery fields (Li et al. 2016). However, this setup was inherently non-cylindrical and the jet was unstable due to magnetohydrodynamic (MHD) and geometric effects. While this experiment was relevant to studying the kinks of the Crab pulsar jet, most long narrow astrophysical jets appear to be stable. Consequently, the dynamics and long-range stability of cylindrical jets cannot be faithfully studied using the V-foil collision platform. The magnetized jets created using a hollow ring of laser beams irradiating flat targets reported here are inherently cylindrical and stable to first order, and exhibit well-defined scaling properties with the ring radius. As we will discuss below, hollow-ring-laser-driven jets have many special and desirable properties not found in jets created using these other schemes. Hence, the hollow-ring-laser jet-launching platform presented here is complementary to previous jet-launching mechanisms.

Our OMEGA experiment was originally motivated by 2D cylindrical FLASH[8] (https://flash.uchicago.edu) simulations (Fryxell et al. 2000), which showed that a hollow-ring-laser jet can reach much higher density and temperatures along the jet axis due to radial compression and heating of the convergent on-axis flow (Fu et al. 2013), compared to outflows launched by the same laser beams irradiating a single spot on the target. The narrow collimation of these hollow-ring-laser jets was achieved by "inertial confinement" analogous to rocket nozzles, not by radiative collapse. Furthermore, a hollow-ring-laser jet was shown to create and sustain magnetic fields far from the target (Fu et al. 2015). When the ring-shaped blow-off collides along the axis, non-parallel gradients in electron density n_e and electron pressure P_e naturally produce "Biermann battery" (Biermann 1950) magnetic fields along the axis. The larger the hollow ring radius, the stronger the field becomes and the farther it extends from the target (Fu et al. 2015). To demonstrate this hollow-ring-laser magnetized jet concept, we carried out a series of experiments in 2015 and 2016 at the OMEGA laser facility of LLE (Boehly et al. 1995). 20 beams of 500 J each from the upper hemisphere of the OMEGA facility were arranged to form a ring pattern at the flat CH target at laser intensities $>10^{14}$ W cm^{-2} (Figure 1), with ring radius d ranging from 0 to 1200 μm. We used proton radiography (P-rad; Li et al. 2006; Zylstra et al. 2012; Gao et al. 2012) to diagnose the magnetic field, optical Thomson scattering (TS; Mackinnon et al. 2004; Froula et al. 2006; Katz et al. 2012; Follett et al. 2016) to measure the plasma and flow parameters at the target chamber center (TCC; 2.5 mm above target, Figure 1), and time-lapse imaging with an X-ray framing camera (XRFC; Bradley et al. 1995; Benedetti et al. 2012) to image the jet emission. The experimental setup is sketched in Figure 1.

2. Results on Magnetic Fields

The most interesting and important results come from the magnetic field diagnostics. Figure 2 shows raw P-rad images from laser rings of radius $d = 0$, 400, 800, and 1200 μm. As the radius d increases, the magnetic fields appear stronger, more collimated, and extend out further, up to ~5 mm for $d = 1200$ μm. The light and dark patterns, created by proton deflections, correspond to net positive and negative currents

[8] FLASH4 is available at https://flash.uchicago.edu/.

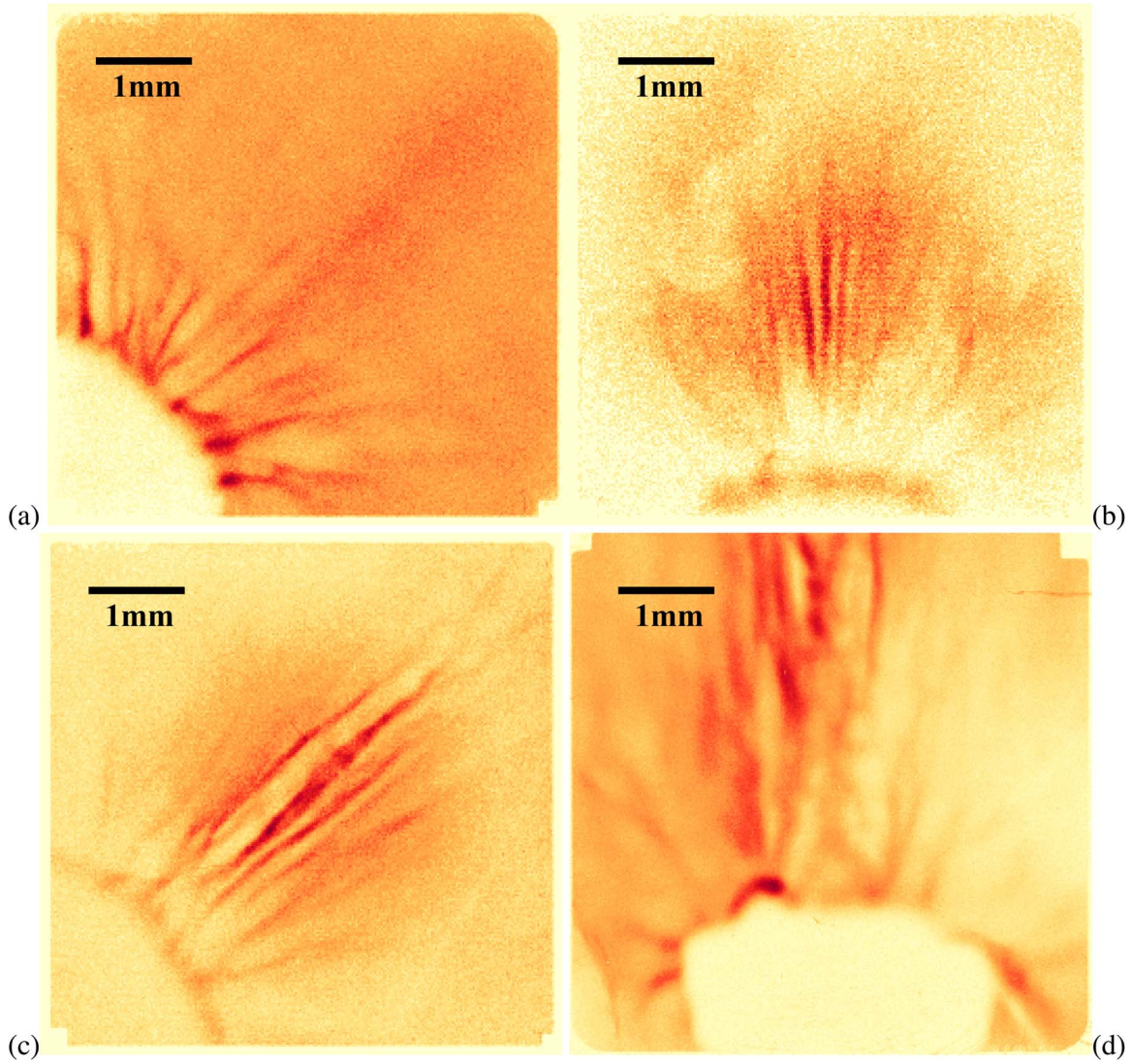

Figure 2. Comparison of P-rad images for jets launched by four different ring-laser radii d: (a) $d = 0$, $t = 3.6$ ns; (b) $d = 400$ μm, $t = 2.6$ ns; (c) $d = 800$ μm, $t = 3.6$ ns; (d) $d = 1200$ μm, $t = 4.3$ ns. All images are those of 14.7 MeV protons. The circular cutoff at the bottom corresponds to the edge of the target.

projected along the line of sight into and out of the plane (Kugland et al. 2012; Graziani et al. 2016; Bott et al. 2017). Vertical proton image filaments correspond to B_z fields, while Y-shaped branches are mainly caused by B_ϕ fields viewed at a slant angle. As the ring radius d is increased, stronger fields are created further from the target and more concentrated along the axis. Even though the 3D magnetic field geometry cannot be uniquely inferred from the 2D proton images, we can still constrain the $\boldsymbol{B}$ field components orthogonal to and integrated along the line of sight, using direct inversion techniques (Graziani et al. 2016; Bott et al. 2017). Figure 3 gives a sample direct inversion result for the transverse $|\boldsymbol{B}|$ of the $d = 800$ μm jet at 3.6 ns along the line-out in blue. Because the physical width of the jet deduced from X-ray images is <1.1 mm, we conclude that the maximum transverse $|\boldsymbol{B}|$ field (central spike in Figure 3(c)) must exceed an MG.

Below we present the simulated P-rad images of the $d = 800$ μm jet using $\boldsymbol{B}$-fields predicted by 3D FLASH simulations. Details of the simulations will be reported elsewhere (Lu et al. 2019). The generalized Ohm's law (Krall & Trivelpiece 1973; Epperlein 1984; Epperlein & Haines 1986) used in the FLASH code includes advection, diffusion, and Biermann battery terms (c = light speed, e = electron charge):

$$\frac{\partial \boldsymbol{B}}{\partial t} = \nabla \times (u \times \boldsymbol{B}) - c\nabla \times (\eta \boldsymbol{j}) + c\frac{\nabla P_e \times \nabla n_e}{e n_e^2} \quad (1)$$

where u = flow advection velocity, η = electrical resistivity, P_e = electron pressure, and n_e = electron density. Figure 4(a) shows $|\boldsymbol{B}|$ profiles at 3 ns predicted by FLASH for four different ring radii d. As d is increased, the maximum field increases and becomes more parallel and concentrated toward the axis, consistent with the P-rad images of Figure 2. The maximum FLASH-predicted fields reach ~MG for $d = 800$ μm and 1200 μm, also consistent with the direct inversion results (Figure 3). Detailed field line plots of the $d = 800$ μm jet (Figure 4(b)) show that they are dominated by poloidal B_z (// to the jet axis) fields near the jet axis and by azimuthal B_ϕ fields (around the jet axis) near the target surface. Figure 4(c) compares the FLASH-simulated P-rad images (left column) with the observed images (right column) at different times, showing good agreement. Both the spacing and contrast of the bright and dark

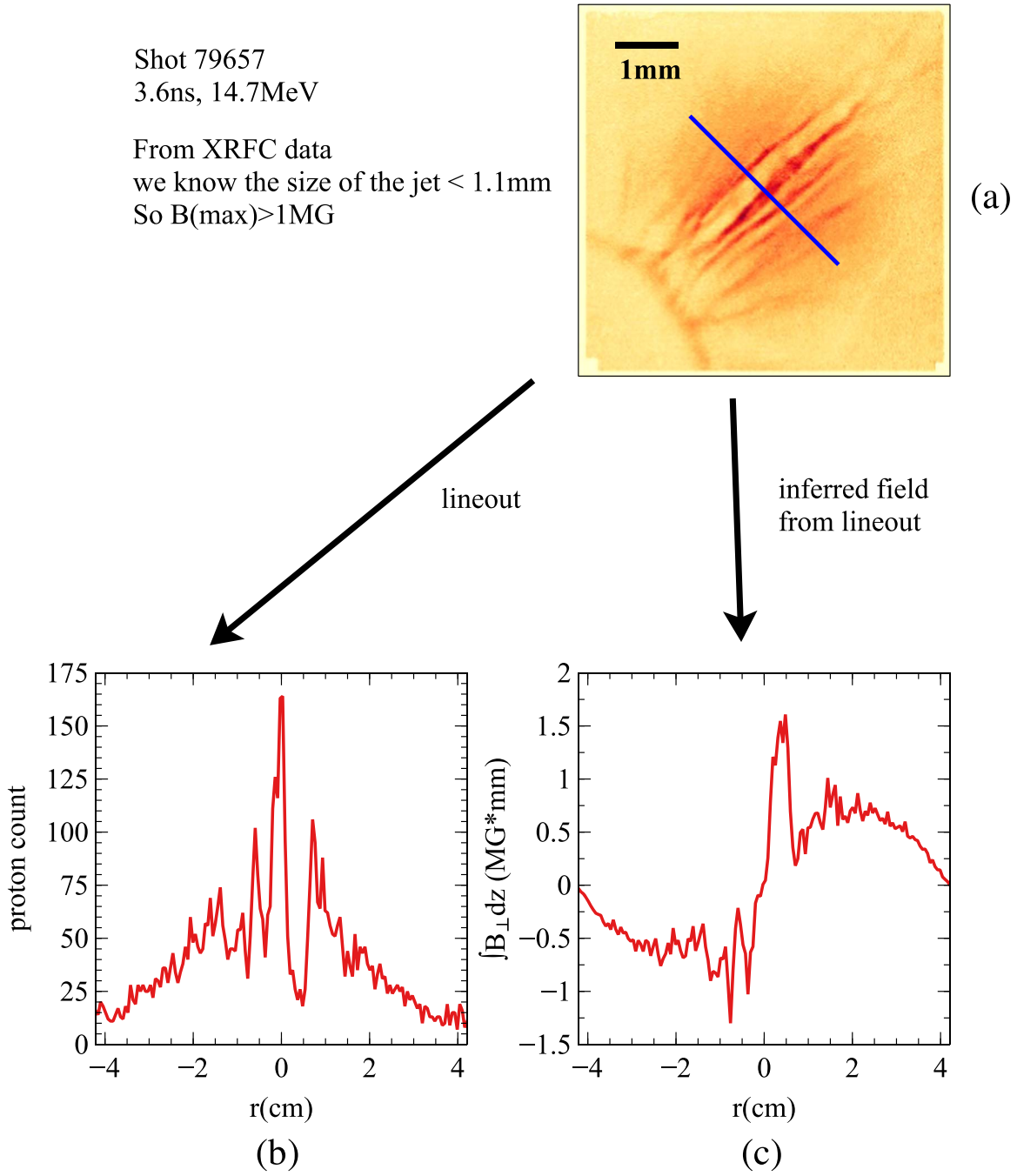

Figure 3. Cross section of integrated transverse $\boldsymbol{B}$-field profile (c) of the $d = 800$ mm jet obtained from the direct inversion of the proton density profile (b), corresponding to the line-out in blue of the P-rad image (a).

streaks, which are sensitive to absolute field amplitudes, are consistent between FLASH simulation and experiment.

Detailed analysis suggests that the primary cause of seed field generation is the collisions between blow-offs from individual laser spots, which create non-parallel density and temperature gradients on the scale of the laser spot radius $r \sim 125\ \mu$m. These filamentary seed fields are then advected toward the jet axis and compressed, producing the strongest fields near the axis (Figures 4(a) and 4(b)). When the ring radius d increases, there is more room for radial advection and compression, leading to stronger and more collimated $\boldsymbol{B}$ fields (Figure 4(a)). At late times, the fields are dominated by a few para-axial bundles with $|B_z| > |B_r|, |B_\phi|$ (Figure 4(b)), which result in the proton images that we see in Figures 2 and 4(c). Thus we have demonstrated the creation of cylindrical plasma jets with self-generated MG fields extending to >4 mm along the jet axis. The amplitude and geometry of these fields can be manipulated by dialing the ring radius and laser parameters.

We can obtain order-of-magnitude estimates of the maximum B-field near the jet axis from dimensional analysis using Equation (1), by balancing the advection term with the Biermann battery term, because the diffusion term is negligible in this case. We find $B_{\max} \sim (\mathrm{cd/eu})(\mathrm{k}T_e/\mathrm{r}^2)$, where $u =$ radial advection velocity $\sim$ ion thermal velocity $\sim (kT_i/Am_p)^{1/2}$, $k =$ Boltzmann constant, $m_p =$ proton mass, and $A = 6.5$ for CH. Therefore, $B_{\max} \sim \mathrm{MG}\ \ (d/800\ \mu\mathrm{m})\ \ (T_e/\mathrm{keV})(T_i/A/\mathrm{keV})^{-1/2}$, in good

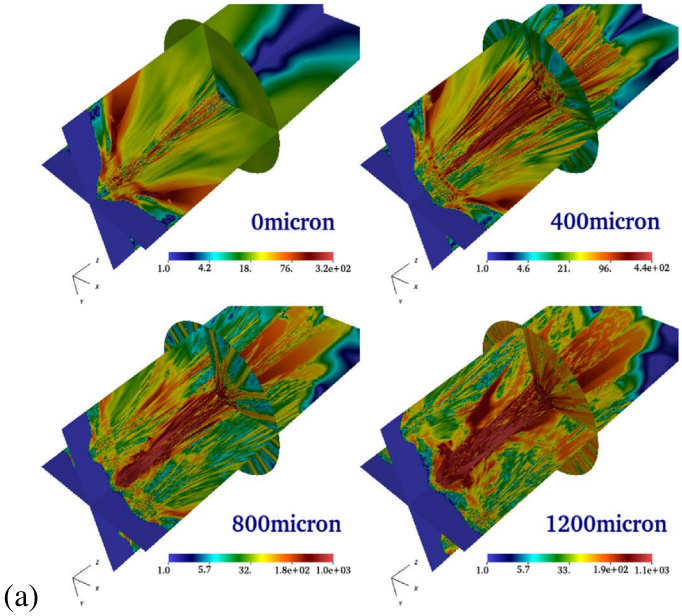

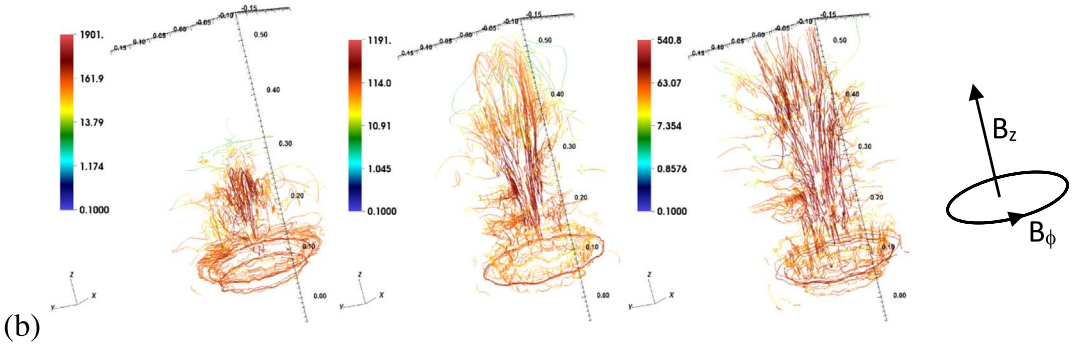

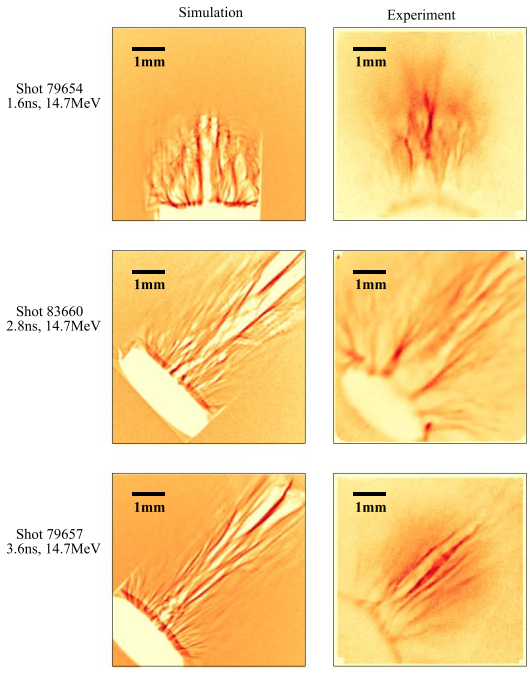

Figure 4. (a) Comparison of 3D FLASH simulations for $|\mathbf{B}|$ profiles at 3 ns for four different ring-jet radii d. (b) Sample field lines at $t = 1.6$ ns, 2.8 ns, and 3.6 ns of the $d = 800$ μm jet. Color scales denote field amplitudes in kG. By symmetry, B_z dominates near the jet axis, while B_ϕ dominates near the target surface. (c) Comparison of 3D FLASH-predicted P-rad images (left column) and observed D^3He P-rad data (right column) for the $d = 800$ μm jet, at the same times as Figure 4(b).

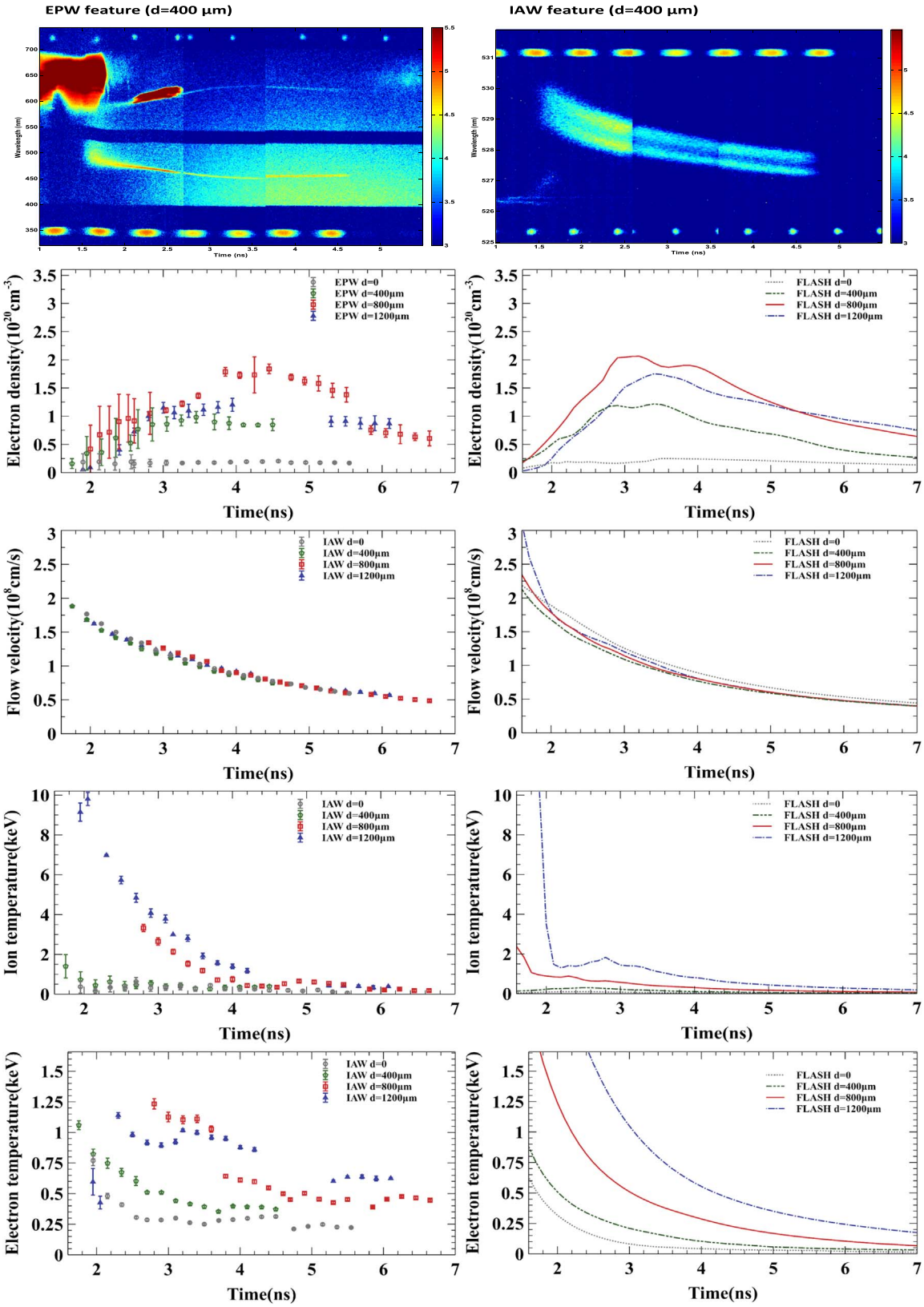

Figure 5. Top row: TS electron plasma wave (EPW) and ion acoustic wave (IAW) spectra vs. time for the $d = 400$ μm jet (combination of 3 shots). Left column, rows 2 to 5: time histories for density, flow velocity, and ion and electron temperatures at TCC for jets of different ring radii d derived from TS spectra. Right column, rows 2 to 5: time histories for density, flow velocity, and ion and electron temperatures at TCC based on 3D FLASH simulations.

agreement with both the direct inversion results (Figure 3) and 3D FLASH predictions (Figure 4(a)). This scaling formula suggests that B_{max} can be increased by increasing d or T_e (which increases with laser intensity). We also note that in our previous 2D simulations (Fu et al. 2015), because of the assumption of perfect cylindrical symmetry, the only gradient length scale is d. Replacing

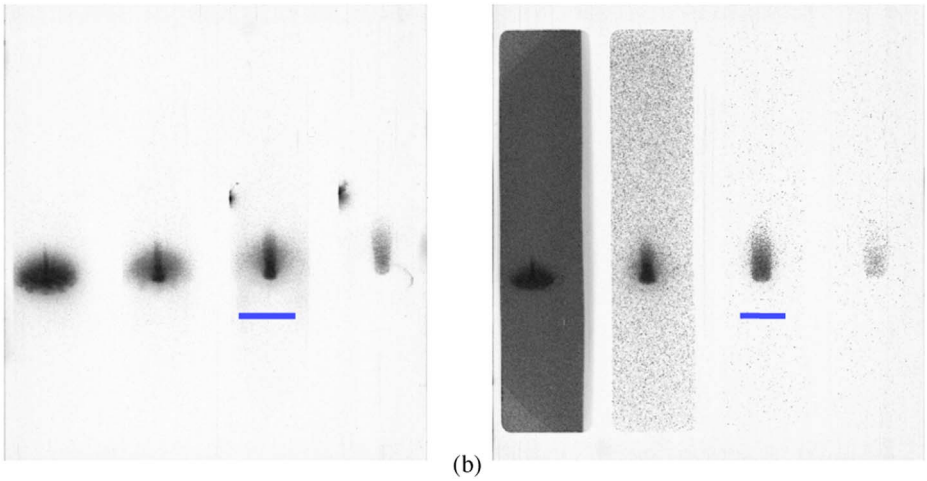

Figure 6. Time-lapse XRFC images (500 ps exposure) of $d = 800$ μm jets for (a) 2% Fe-doped CH target and (b) pure CH target. In (a) the frames are taken at 2 , 3, 4, and 5 ns. In (b) the frames are taken at 2, 2.5, 3, and 4 ns. The blue marker in each picture denotes a length of 1.6 mm. It is clear that the Fe-doped jet appears narrower than the pure CH jet.

Table 1
Measured Parameters of the $d = 800$ μm jet at 3.5 ns and 2.5 mm from Laser Target On-axis (Left Column) Compared to those of YSO Jets (Right Column)

$d = 800$ μm OMEGA Jet	YSO Jet
Electron density $n_e \sim 1.5 \times 10^{20}$ cm^{-3}	$\sim 10^2$–10^5 cm^{-3}
Electron temperature $T_e \sim 1$ keV	$\sim 10^4$ K-few $\times$ 10^6 K
Ion temperature $T_i \sim 2.5$ keV	$\sim T_e$
Ionization $\langle Z \rangle \sim 3.5$	low-100%
Flow velocity $v \sim 1.2 \times 10^8$ cm s^{-1}	$\sim$few $\times$ 10^7 cm s^{-1}
Magnetic field $B \sim 10^6$ Gauss	$\sim$20–500 μG
Plasma beta $\beta = 8\pi P_g/B^2 \sim 10$	$\sim$10–10^3
Mach number $M = v/c_s \sim 3$	few-10
Alfvén Mach number $M_A = v/v_A \sim 8$	$\sim 10^2$
Reynolds number $R_e \sim 10^4$	$\sim$10–10^3
Magnetic Reynolds number $R_{eM} \sim 10^4$	$\sim$few $\times$ 10^2
Peclet number $P_{e\|\|} = 1.5\ kn_e vR/\kappa_{T\|\|B} \sim 0.3$	unknown
$P_{e\ orth} = 1.5\ kn_e vR/\kappa_{T\ orth\ B} \sim 30$	unknown
Hydro time/Rad. cooling time (CH) ~ 0.01	various
Hydro time/Rad. cooling time (2%Fe) ~ 1	
Electron skin depth $c/\omega_e \sim 0.4$ μm	
Ion skin depth $c/\omega_I \sim 24$ μm	
Debye length $v_e/\omega_e \sim 0.01$ μm	
Electron gyroradius $v_e/\omega_{Be} \sim 0.6$ μm	
Ion gyroradius $v_i/\omega_{Bi} \sim 20$ μm	
Coulomb scattering mean free path $\lambda_{ei} \sim 20$ μm	

d/r^2 with $1/d$ in the equation above, we obtain $B_{max} \sim 25$ kG for $d = 800$ μm, again in good agreement with 2D FLASH predictions (Fu et al. 2015). The difference in the magnitude of B_{max}, a 2D-cylindrical Biermann battery, can only generate B_ϕ field (Fu et al. 2015), whereas the 3D Biermann battery field is complex and dominated by B_z near the axis (Figure 4(b)). We emphasize that simulated P-rad images using 25 kG pure B_ϕ fields completely disagree with the observed images (Figures 2 & 4(c)).

3. Plasma Parameters and Jet Morphology

The time histories of density, temperatures, and velocity at TCC were measured using optical TS (Mackinnon et al. 2004; Froula et al. 2006; Katz et al. 2012) with a $2\omega_o$ ($\lambda_o = 526.5$ nm) probe beam. Figure 5 compares the experimental data derived from TS with 3D FLASH predictions. The plasma parameters were inferred from the TS spectra from electron plasma waves and ion acoustic waves, using the technique discussed in Follett et al. (2016). Comparing with FLASH predictions, the agreements for electron density and flow velocity are excellent, and the qualitative trends for T_i and T_e are basically consistent. However, we still need to improve the temperature calculations in FLASH to get better quantitative agreement with the temperatures inferred from TS (Lu et al. 2019). Both simulation and experimental data suggest that the $d = 800$ μm jet achieves the highest maximum density on-axis, whereas the $d = 1200$ μm jet achieves the highest maximum temperature on-axis, respectively.

Evolution of the global jet morphology was observed using time-lapse X-ray imaging with an XRFC (Bradley et al. 1995; Benedetti et al. 2012) located at 38° from the jet axis. Figure 6 compares the evolution of two $d = 800$ μm jets, one with 2% Fe-doped CH target (Figure 6(a)), and one with pure CH target (Figure 6(b)). Both jets are well collimated and stable, but the Fe-doped jet appears even narrower than the pure CH jet due to stronger radiative cooling, consistent with FLASH predictions. In principle, these X-ray images can be used to constrain the density and temperature profiles if the X-ray intensities were absolutely calibrated. Unfortunately, absolute calibration of the X-ray cameras was not performed for these experiments due to the lack of times. We plan to do it for future experiments.

4. Discussions and Astrophysical Applications

Our method of creating strongly magnetized cylindrical jets using a ring of multiple laser beams is ideal for scaling up to larger platforms by using more lasers and higher-intensity beams, such as those available at the National Ignition Facility (NIF) at Livermore, California. In terms of magnetic fields, the key advantage of using more laser beams (e.g., up to 64 beams at NIF) is to make the hollow ring pattern larger and more uniform. A larger ring creates stronger fields due to more room for radial compression (see B_{max} formula in Section 2), and a more uniform ring produces larger pitch angle $|B_\phi/B_z|$, because a higher degree of azimuthal symmetry enhances B_ϕ and reduces B_z (see Equation (1)). Future FLASH simulations will quantify the effects of the ring radius and number of laser beams on $|B_\phi/B_z|$, which

plays important roles in the stability of the jet (Krall & Trivelpiece 1973). In addition to modeling astrophysical jets, supersonic outflows with well-characterized ordered magnetic fields can be used to study magnetized shocks (Sironi & Spitkovsky 2009), shear boundaries, reconnection, and other plasma processes via interactions with an opposing jet (Park et al. 2012; Ross et al. 2012; Fox et al. 2013; Huntington et al. 2015), ambient media, and external B-fields.

To address the relevance of our ring-laser jets to astrophysical jets, we present in Table 1 representative physical parameters of the $d = 800\ \mu$m ring jet at 3 ns and 2.5 mm from the laser target. As these hydrodynamic jets are kinetic dominated (in contrast to magnetic-dominated or magnetic tower jets driven by pulse power), they are most relevant to the study of young stellar object (YSO) jets (Frank et al. 2014). Table 1 shows that most dimensionless parameters for both types of jets (plasma β, Mach number, Alfvén Mach number, Reynolds number, and magnetic Reynolds number) lie in the same regime, suggesting the scalability of important properties of the hollow-ring-laser jets to the astrophysical regime (Ryutov et al. 1999, 2000). It has been proposed that the stability of some YSO jets may be caused or enhanced by strong poloidal magnetic fields (Albertazzi et al. 2014). Because our hollow-ring-laser jet is created with strong poloidal fields near the axis (Figure 4), it is a useful platform to study the stabilizing effects of strong poloidal magnetic fields on the propagation of YSO jets. As the density, temperature, flow speed, and magnetic field of the ring-laser jet can be varied in a controllable manner by dialing the ring radius and laser parameters, a broad range of YSO jets with matching dimensionless parameters can be studied with such experiments (Frank et al. 2014).

The ring-laser-jet platform can be readily expanded in several new directions. For example, most early laboratory experiments to study YSO jets used metal targets so that radiative cooling dominates the jet collimation and dynamics (e.g., the PALS experiments, see Section 1), whereas radiative cooling was dynamically unimportant in our pure CH jets (Table 1). However, by adding high-Z dopants to our CH target (Figure 6), we can increase radiative cooling (Table 1) to increase the aspect ratio (L/R) of the hollow-ring-laser jet (Figure 6), consistent with previous PALS experiments (Kasperczuk et al. 2006; Nicolaï et al. 2006). Radiative cooling may also reduce the plasma $\beta(=p_{\rm gas}/p_{\rm B})$ to reach the low-β regime, which should lead to interesting new physics. Consequently, the role of radiative cooling in the diversity of YSO jet morphology (Frank et al. 2014) may be studied in the laboratory by varying the high-Z dopant level.

The ring configuration is also ideal for adding angular momentum to the jet by using tilted-tile target surfaces, so that the blow-off from each individual laser spot becomes slanted. Finally, we can replace the flat target with cone-shaped or bowl-shaped targets. Depending on the opening angle of the cone or the curvature of the bowl, the increased convergence of the on-axis flow can potentially lead to even stronger magnetic field, higher density, temperature, and flow speed than the values listed in Table 1, and all these parameters can be varied experimentally by changing the target shape and composition together with ring radius and laser parameters. Comparing the ring-laser jets with jets launched by other platforms, we see that the ring-laser jet parameters have a larger dynamic range. This increased dynamic range should benefit the laboratory study of a broad range of YSO jets.

Another important and novel property of these kinetic-dominated but strongly magnetized jets is their thermal conductivity (Braginskii 1958; Spitzer 2006). Electron transport in these jets becomes highly anisotropic due to the strong fields and small gyroradii (Table 1). As a result, electron heat conduction is suppressed orthogonal to $\boldsymbol{B}$ (Braginskii 1958), but remains Spitzer-like parallel to $\boldsymbol{B}$ (Spitzer 2006), leading to steeper gradient for the electron temperature in the radial direction but less steep gradient in the axial direction (Figure 4(b)). In addition, the Righi-Leduc term can transport electron energy in azimuthal direction and create azimuthal variation of electron temperature. The Nernst term can slow down the B field advection into the hot region (Gao et al. 2015). Future FLASH predictions including anisotropic thermal conduction and Nernst effect should be testable using our TS and XRFC data, plus other diagnostics. The role of thermal conduction is an outstanding unsolved problem in many fields of astrophysics, including YSO jets. Our ring-laser jet can thus provide a new experimental test bed for theories of magnetized thermal conduction relevant to both laboratory and astrophysical plasmas.

This research was supported by DOE NNSA Grant DE-NA0002721. FLASH simulations were performed on Extreme Science and Engineering Discovery Environment (XSEDE), which is supported by National Science Foundation grant number ACI-1548562, and the Argonne Leadership Computing Facility, which is a DOE Office of Science User Facility supported under Contract DE-AC02-06CH11357. Proton radiography was supported in part by DOE Grant No. DE-FG03-09NA29553, No.DE-SC0007168. E.L. and Y.L. acknowledge partial support by LANL/LDRD during the writing of this Letter.

References

Albertazzi, B., Ciardi, A., Nakatsutsumi, M., et al. 2014, Sci, 346, 325
Bally, J., Reipurth, B., & Davis, C. J. 2007, Protostars and Planets V (Tuscon, AZ: Univ. Arizona Press), 215
Benedetti, L. R., Bell, P. M., Bradley, D. K., et al. 2012, RScI, 83, 10E135
Biermann, L. 1950, ZNatA, 5, 65
Boehly, T. R., Craxton, R. S., Hinterman, T. H., et al. 1995, RScI, 66, 508
Bott, A., Graziani, C., Tzeferacos, P., & White, T. G. 2017, JPlPh, 83, 2017
Bradley, D. K., Bell, P. M., Landen, O. L., et al. 1995, RScI, 66, 716
Braginskii, S. I. 1958, JETP, 6, 358
Ciardi, A. (ed.) 2015, in HEDLA X Conf. Proc. 17, High Energy Density Physics,Part A, special issue (Amsterdam: Elsevier)
Epperlein, E. M. 1984, JPhD, 17, 1823
Epperlein, E. M., & Haines, M. G. 1986, PhFl, 29, 1029
Farley, D. R., Estabrook, K. G., Glendinning, S. G., et al. 1999, PhRvL, 83, 1982
Ferrari, A. 1998, ARA&A, 36, 539
Follett, R. K., Delettrez, J. A., Edgell, D. H., et al. 2016, RScI, 87, 11E401
Fox, W., Fiksel, G., Bhattacharjee, A., et al. 2013, PhRvL, 111, 225002
Frank, A., Ray, T. P., Cabrit, S., et al. 2014, in Protostars and Planets VI, ed. H. Beuther et al. (Tuscon, AZ: Univ. Arizona Press), 451
Froula, D. H., Ross, J. S., Divol, L., & Glenzer, S. H. 2006, RScI, 77, 10E522
Fryxell, B., Olson, K., Ricker, F. X., et al. 2000, ApJS, 131, 273
Fu, W., Liang, E., Tzeferacos, P., & Lamb, D. 2015, HEDP, 17, 42
Fu, W., Liang, E. P., Fatenejad, M., et al. 2013, HEDP, 9, 336
Gao, L., Nilson, P. M., Igumenschev, V., et al. 2012, PhRvL, 109, 115001
Gao, L., Nilson, P. M., Igumenschev, I. V., et al. 2015, PhRvL, 114, 215003
Gourdain, P.-A., Blesener, I. C., Greenly, J. B., et al. 2010, PhPl, 17, 012706
Graziani, C., Tzeferacos, P., Lamb, D., & Li, CK. 2017, RScI, 88, 123507
Gregory, C. D., Howe, J., Loupias, B., et al. 2008, ApJ, 676, 420
Hartigan, P. 2013, in HEDLA IX Conf. Proc. 9, High Energy Density Physics, Special Issue, ed. P. Hartigan (Amsterdam: Elsevier)
Huntington, C. M., Fiuza, F., Ross, J. S., et al. 2015, NatPh, 11, 173
Kasperczuk, A., Pisarczyk, T., Borodziuk, S., et al. 2006, PhPl, 13, 062704
Katz, J., Boni, R., Sorce, C., et al. 2012, RScI, 83, 10E349
Krall, N., & Trivelpiece, A. 1973, Principles of Plasma Physics (New York: McGraw Hill)

Kugland, N., Ryutov, D., Plechaty, C., Ross, J., & Park, H. S. 2012, RScI, 83, 101301
Lebedev, S. V., Chittenden, J. P., Beg, F. N., et al. 2002, ApJ, 564, 113
Lebedev, S. V., Ciardi, A., Ampleford, D. J., et al. 2005, MNRAS, 361, 97
Li, C. K., Séguin, F. H., Frenje, J. A., et al. 2006, PhRvL, 97, 135003
Li, C. K., Tzeferacos, P., Lamb, D., et al. 2016, NatCo, 7, 13081
Livio, M. 1999, PhR, 311, 225
Lu, Y., Tzeferacos, P., Liang, E., et al. 2019, PhPl, 26, 022902
Mackinnon, A. J., Shiromizu, S., Antonini, G., et al. 2004, RScI, 75, 3906
Nicolaï, Ph., Stenz, C., Kasperczuk, A., et al. 2008, PhPl, 15, 082701
Nicolaï, Ph., Tikhonchuk, V. T., Kasperczuk, A., et al. 2006, PhPl, 13, 062701
Park, Hye-Sook, Ryutov, D. D., Ross, J. S., et al. 2012, HEDP, 8, 38
Pisarczyk, T., Kasperczuk, A., Krousky, E., et al. 2007, PPCF, 49, B611
Ross, J. S., Glenzer, S. H., Amendt, P., et al. 2012, PhPl, 19, 056501
Ryutov, D., Drake, R. P., Kane, J., et al. 1999, ApJ, 518, 821
Ryutov, D., Drake, R., & Remington, B. 2000, ApJS, 127, 465
Sari, R., Piran, T., & Halpern, J. P. 1999, ApJL, 519, L17
Sironi, L., & Spitkovsky, A. 2009, ApJL, 707, L92
Spitzer, L. 2006, Physics of Fully Ionized Gases (New York: Dover)
Suzuki-Vidal, F., Lebedev, S. V., Bland, S. N., et al. 2011, Ap&SS, 336, 41
Tikhonchuk, V. T., Nicolaï, Ph., Ribeyre, X., et al. 2008, PPCF, 50, 124056
Zylstra, A. B., Li, C. K., Rinderknecht, H. G., et al. 2012, RScI, 83, 013511